

CtrlFuse: Mask-Prompt Guided Controllable Infrared and Visible Image Fusion

Yiming Sun¹, Yuan Ruan¹, Qinghua Hu², Pengfei Zhu^{1,3,4*}

¹School of Automation, Southeast University, Nanjing, China

²School of Artificial Intelligence, Tianjin University, Tianjin, China

³Low-Altitude Intelligence Laboratory, Xiong'an National Innovation Center, Xiongan, China

⁴Xiong'an Guochuang Lantian Technology Co., Ltd., Xiongan, China

{sunyiming, ruanyuan}@seu.edu.cn, {huqinghua, zhupengfei}@tju.edu.cn

Abstract

Infrared and visible image fusion generates all-weather perception-capable images by combining complementary modalities, enhancing environmental awareness for intelligent unmanned systems. Existing methods either focus on pixel-level fusion while overlooking downstream task adaptability or implicitly learn rigid semantics through cascaded detection/segmentation models, unable to interactively address diverse semantic target perception needs. We propose CtrlFuse, a controllable image fusion framework that enables interactive dynamic fusion guided by mask prompts. The model integrates a multi-modal feature extractor, a reference prompt encoder (RPE), and a prompt-semantic fusion module (PSFM). The RPE dynamically encodes task-specific semantic prompts by fine-tuning pre-trained segmentation models with input mask guidance, while the PSFM explicitly injects these semantics into fusion features. Through synergistic optimization of parallel segmentation and fusion branches, our method achieves mutual enhancement between task performance and fusion quality. Experiments demonstrate state-of-the-art results in both fusion controllability and segmentation accuracy, with the adapted task branch even outperforming the original segmentation model.

Code — <https://github.com/Sevryy/CtrlFuse>

Introduction

Infrared and visible image fusion aims to combine complementary information from both modalities to generate comprehensive representations of scenes (Ma et al. 2016; Tang, Li, and Ma 2025), thereby enhancing the environmental perception capabilities of intelligent unmanned systems from night to day (Sun et al. 2024a, 2025). Although visible images provide rich color information and high spatial resolution, their performance in downstream tasks degrades under poor illumination conditions. Infrared images effectively compensate for the limitations of visible imaging in darkness through thermal target imaging, but lack texture information of targets, leading to misidentification issues in downstream applications. How to better leverage the advantages of both imaging modalities to improve various downstream applications has become a key research focus.

*Corresponding author
Copyright © 2026, Association for the Advancement of Artificial Intelligence (www.aaai.org). All rights reserved.

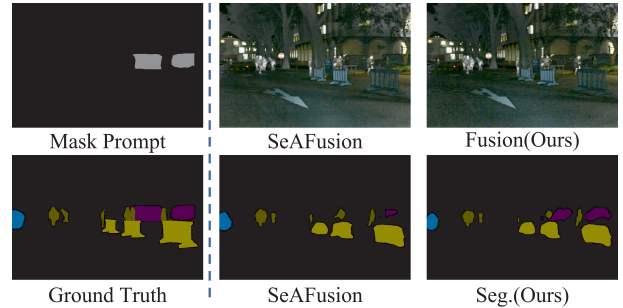


Figure 1: The importance of mask prompt-based interactive controllable image fusion for the performance of downstream application models (e.g., semantic segmentation).

With the development of deep learning, several representative infrared and visible image fusion methods have emerged (Cao et al. 2023). Autoencoder-based methods enhance fusion performance through multi-scale feature decomposition or pretraining-finetuning strategies. Generative adversarial network (GAN)-based (Ma et al. 2020) approaches preserve effective information from different modalities by establishing adversarial learning between fused images and multimodal source images. Beyond CNN-based methods, transformer architectures and diffusion models (Tang et al. 2024) have also attracted researchers' attention. Traditional image fusion tasks primarily focus on pixel-level consistency between fused and source images, evaluating performance through image quality assessment metrics, while neglecting the crucial requirement that fused images should effectively serve downstream perception tasks for improved task performance.

In recent years, researchers have recognized this need, leading to the proposal of task-related multimodal image fusion methods (Tang et al. 2025b; Liu et al. 2024a). These approaches connect image fusion networks with downstream task networks (e.g., object detection or semantic segmentation models) through joint optimization, enabling fusion models to implicitly learn semantically relevant information for downstream tasks. However, this paradigm severely restricts the fusion model's semantic perception capability to the predefined recognition types of the cascaded down-

stream task model, failing to dynamically control the attention to specific targets according to varying application requirements. As shown in Fig. 1, although existing methods have learned target semantics during training, they still struggle to adapt to real-world vehicle segmentation scenarios. Our method significantly enhances the semantic segmentation capability for designated targets (Car) through controllable prompt guidance, improving the practicality of task-driven image fusion models. Therefore, constructing semantically controllable multimodal image fusion architectures that enable dynamic controllable fusion according to different semantic requirements could bridge high-level downstream applications with low-level image fusion tasks.

In this paper, we propose a controllable image fusion method with multimodal semantic-aware prompt tuning (CtrlFuse), establishing a semantic-guided controllable multimodal image fusion framework through prompt tuning of the foundation model with superior semantic perception capability (Segment Anything Model (Kirillov et al. 2023), SAM). Specifically, the proposed CtrlFuse consists of four components: a multimodal backbone encoder-decoder, a reference prompt encoder (RPE), a prompt semantic fusion module (PSFM), and the pre-trained SAM. In the proposed RPE, we construct support features and query features that form prompt features for SAM fine-tuning under mask guidance. The PSFM explicitly fuses semantic prompt features, segmentation masks from SAM, and multimodal features from the encoder, achieving dynamic explicit injection of semantic information. Our method enhances performance on multimodal image fusion tasks by jointly optimizing the loss functions for both the SAM task branch and the image fusion branch. The main contributions are summarized as follows:

- We propose an interactively controllable multimodal image fusion framework that establishes a concise controllable fusion paradigm through dynamic mask prompts and explicit fusion of multimodal features with foundation model fine-tuning.
- We design a reference prompt encoder to dynamically generate semantic prompts for SAM fine-tuning, and develop a prompt semantic fusion module to explicitly aggregate semantic prompts with multimodal features, enhancing semantic perception capability.
- Extensive experiments validate the superior fusion performance and semantic controllability of our method. In particular, our approach achieves enhanced fusion capability through multimodal semantic fine-tuning, revealing the synergistic advantage of mutual promotion between the fusion and segmentation tasks.

Related Works

Infrared and Visible Image Fusion integrates complementary multi-modal features to preserve salient information from both sources (Ma, Ma, and Li 2019; Zhang et al. 2021; Liu et al. 2025). Ma et al. (Ma et al. 2019) proposed Fusion-GAN to formulate the image fusion task as an adversarial game between preserving infrared thermal radiation and visible texture details. Zhao et al. (Zhao et al. 2020) proposed a deep image decomposition framework that separates source

images into background and detail feature maps, followed by dedicated fusion strategies for each feature. Li et al. (Li, Wu, and Durrani 2020) proposed a fusion network featuring nested connectivity to achieve multi-scale fusion of multimodal images. Recently, some task-driven methods have also attracted wide attention. Sun et al. (Sun et al. 2022a) proposed a detection-driven network for infrared and visible image fusion that leverages target-specific features from object detection tasks to guide the fusion process. Liu et al. (Liu et al. 2022) proposed a fusion framework that enhances object detection performance through dual adversarial optimization. Tang et al. (Tang, Yuan, and Ma 2022) proposed a semantic-aware fusion network that cascades the fusion module with a semantic segmentation module to enhance fusion performance. Yi et al. (Yi et al. 2024) proposed a text-guided image fusion framework that utilizes prompts to enable degradation-aware fusion. However, existing task-driven methods typically cascade image fusion with downstream application tasks, with high-level visual models (detection or segmentation) guiding the optimization of fusion models. This approach only supports the learning of fixed semantic categories and is difficult to adapt dynamically to complex and diverse semantic category perception requirements. Furthermore, it cannot achieve interactive and controllable fusion.

Interactive Deep Learning Model refers to a class of neural network architectures that enable human-steered regulation of model behavior (Cao et al. 2024; Tang et al. 2025a). Kirillov et al. (Kirillov et al. 2023) proposed the Segment Anything Model (SAM), a general-purpose segmentation system featuring interactive control and strong zero-shot generalization. Based on SAM, many other interactive large models have also been proposed, such as VRP-SAM (Sun et al. 2024b), GroundedSAM (Ren et al. 2024), and SAGE (Wu et al. 2025). In recent years, diffusion models have demonstrated significant progress in controllability (Shi et al. 2024; Zhang and Agrawala 2024; Hoe et al. 2024). Avrahami et al. (Avrahami, Lischinski, and Fried 2022) developed blended diffusion by effectively integrating CLIP’s (Radford et al. 2021) semantic understanding capabilities with diffusion models to achieve text-driven image inpainting. Huang et al. (Huang et al. 2023) proposed a novel paradigm for composable conditional image synthesis that achieves creative controllability while maintaining generation quality. However, existing fusion methods predominantly focus on optimizing quantitative metrics for static outputs, while largely neglecting the development of controllable dynamics. This oversight results in limited adaptability to real-world scenarios requiring interactive adjustment or dynamic responses. Considering that image fusion should ultimately enhance downstream task performance, controllable region-aware fusion enhancement methods would provide greater practical value.

Methods

Overall Architecture

In this paper, we propose a semantic-aware framework enabling controllable fusion via multi-modal prompt tuning,

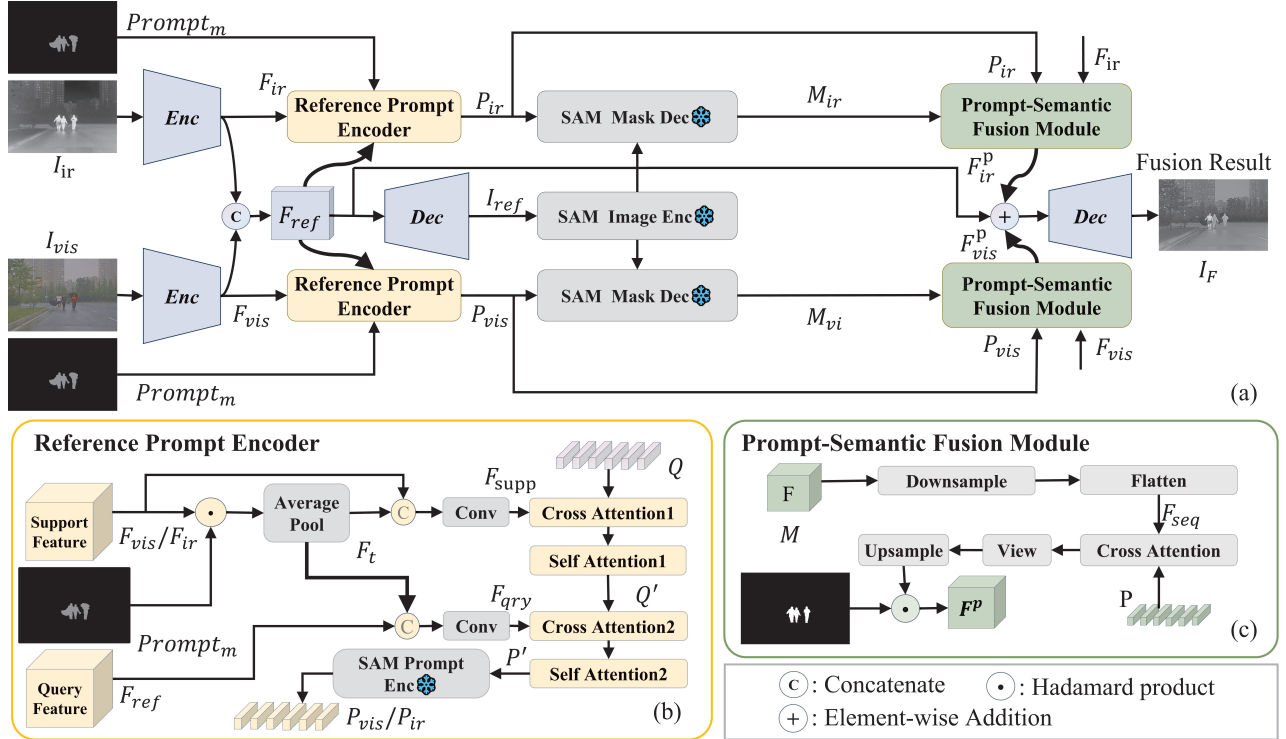


Figure 2: The architecture of CtrlFuse. CtrlFuse consists of two reference prompt encoders, two Prompt-Semantic fusion modules guided by the prompt mask, a set of infrared and visible feature encoders, and the auxiliary network.

termed CtrlFuse. In Fig 2, CtrlFuse contains a Reference Prompt Encoder, a Prompt-Semantic Fusion Module, and the auxiliary network.

In Fig. 2(a), we send a pair of infrared image $I_{ir} \in \mathbb{R}^{1 \times H \times W}$ and visible image $I_{vis} \in \mathbb{R}^{3 \times H \times W}$ into the infrared and visible encoders to extract the features F_{ir} and F_{vis} , respectively. The structure of encoders follows (Tang, Yuan, and Ma 2022). Then we concatenate F_{ir} and F_{vis} into F_{ref} as the input of the image decoder consisting of convolutional layers and activation layers to get the reference image I_{ref} . We send a mask as a prompt into Reference Prompt Encoder along with F_{ir} or F_{vis} and F_{ref} . In the Reference Prompt Encoder, we use F_{ir} or F_{vis} as support feature, F_{ref} as query feature and get prompt feature embedding P_{ir} and P_{vis} , respectively. We then send I_{ref} into the frozen SAM image encoder, and the result is sent to frozen SAM mask decoder with P_{ir} and P_{vis} respectively, after that we get two prediction masks M_{ir} and M_{vis} . To obtain the dual-light prompt features F_{ir}^p and F_{vis}^p , we input the prediction masks, prompt embeddings, and encoded features into the Prompt-Semantic Fusion Module. Through element-wise addition of the preliminary fusion feature F_{ref} with the prompt features F_{ir}^p and F_{vis}^p , the final fusion features are obtained. These final features are subsequently input into the image decoder to generate the ultimate fused image $I_F \in \mathbb{R}^{1 \times H \times W}$.

We train the proposed CtrlFuse model in an end-to-end manner. The model is optimized mainly by calculating both the fusion loss \mathcal{L}_{fusion} and the segmentation loss \mathcal{L}_{seg} .

Reference Prompt Encoder

As shown in Fig. 2(b), we propose a Reference Prompt Encoder to dynamically extract prompt embeddings from the controllable regions of interest.

Taking the infrared reference prompt encoder as an example, we take F_{ir} as a support feature, F_{ref} as a query feature, and input them along with $Prompt_m$ into the encoder. To enhance the features in the regions of interest, we compute the Hadamard product between $Prompt_m$ and F_{ir} , followed by an average pooling operation to get F_t . This process can be described as follows:

$$F_t = \text{AveragePool}(Prompt_m \cdot F_{ir}). \quad (1)$$

In order to achieve a holistic feature representation that captures both detailed local information and global context, which enhances the model's performance and generalization ability, we separately concatenate F_{ir} and F_{ref} with F_t , and then apply convolutional layers to produce the resulting features $F_{supp} \in \mathbb{R}^{C \times H \times W}$ and $F_{qry} \in \mathbb{R}^{C \times H \times W}$. This process can be described as follows:

$$F_{supp} = \text{Conv}(\text{Concat}(F_{ir}, F_t)), \quad (2)$$

$$F_{qry} = \text{Conv}(\text{Concat}(F_{ref}, F_t)). \quad (3)$$

We get a set of learnable queries $Q \in \mathbb{R}^{N \times C}$, that extract different aspects of information from F_{supp} , where N corresponding to the number of prominent features the model focuses on, is set to 40 as determined by hyperparameter experiments. We first pass the queries Q and F_{supp}

through a cross-attention layer, and then feed the resulting output into a self-attention layer to obtain queries that are controllable for specific categories in the support image Q' . Subsequently, Q' and F_{qry} are processed through a cross-attention mechanism. The resulting output is then fed into a self-attention layer to derive a set of reference prompts P' , which correspond to specific categories present in the query image. This process can be described as follows:

$$Q' = \text{SelfAttn}_1(\text{CrossAttn}_1(Q, F_{supp})) \quad (4)$$

$$P' = \text{SelfAttn}_2(\text{CrossAttn}_2(Q', F_{qry})) \quad (5)$$

Then, P' is passed through the frozen SAM Prompt Encoder to generate the final prompt feature embedding P .

Prompt-Semantic Fusion Module

As shown in Fig. 2(c), we propose a Prompt-Semantic Fusion Module to obtain category-specific prompt features F_{ir}^P and F_{vis}^P . In both the infrared and visible branches, the initial encoded features F , the prompt feature embeddings P , and the corresponding SAM segmentation outputs M are used as input representations. Given the notable differences in how various modalities contribute to semantic information, we employ segmentation results derived from each modality-specific branch (e.g., infrared and visible) as masks. Specifically, the quality of the segmentation outcomes directly reflects the richness and quality of the high-level features provided by that modality, thereby indicating its potential contribution to overall task performance. Such a strategy not only facilitates the quantification of each modality's effectiveness but also provides more precise guidance for multi-modal data fusion. First, we downsample the feature map $F \in \mathbb{R}^{H \times W \times C}$ to reduce the computational load of the network. Then, we flatten the downsampled features into a sequence format $F_{seq} \in \mathbb{R}^{(H*W) \times C}$. This process can be described as follows:

$$F_{seq} = \text{Flatten}(\text{Down}(F)) \quad (6)$$

We process the serialized features F_{seq} together with the previously derived prompt embeddings P through a cross-attention mechanism. Subsequently, the attended features are subjected to a view transformation operation to revert to their original spatial dimensions, followed by an upsampling step to restore them to the original resolution, thereby obtaining enhanced spatial features. Finally, these enhanced spatial features are element-wise multiplied with the corresponding segmentation masks to derive the enhanced features specific to the indicated categories. This process can be described as follows:

$$F^P = M \cdot (\text{Up}(\text{View}(\text{CrossAttn}(F_{seq}, P)))) \quad (7)$$

Experiments

Experimental Setting

Implementation Details. We performed experiments on a computing platform with four NVIDIA GeForce RTX 3090 GPUs. We used Adam Optimization to update the overall network parameters with the learning rate of 1.0×10^{-4} . The training epoch is set to 150 and the batch size is 4.

Datasets and Partition Protocol. We conducted experiments on three publicly available datasets: FMB (Liu et al. 2023), MSRS (Tang et al. 2022), and DroneVehicle (Sun et al. 2022b). FMB and MSRS contain labels for semantic segmentation, and we generate masks for different categories from these labels. FMB contains 1,500 infrared-visible image pairs captured by onboard cameras. We used 1,020 pairs of images for training, 280 pairs of images for validation, and the remaining 200 pairs for evaluation. MSRS contains 1,444 infrared-visible image pairs captured by onboard cameras. We used 1,072 image pairs for training, 150 image pairs for validation, and 200 image pairs for evaluation. For DroneVehicle, we generate masks using other semantic segmentation models. We evaluated 200 image pairs from DroneVehicle. We present both qualitative and quantitative analyses of the MSRS dataset in the supplementary material.

Competing Methods. We compared 8 state-of-the-art methods on three publicly available datasets. In these comparison methods, LDfusion (Wang et al. 2024) is the CLIP-based image fusion method, NestFuse (Li, Wu, and Durrani 2020) is the autoencoder-based method, DIDFuse (Zhao et al. 2020) and CDDFuse (Zhao et al. 2023) are the deep learning-based image decomposition methods. SwinFuse (Wang et al. 2022) is a Transformer-based method. SeAFusion (Liu et al. 2022) and SDCFusion (Liu et al. 2024b) are the segmentation-driven methods. PSFusion (Tang et al. 2023) is a fusion method driven by high-level vision tasks.

Evaluation Metrics. We evaluated the performance of the proposed method based on qualitative and quantitative results. The qualitative evaluation is mainly based on the visual effect of the fused image. A good fused image needs to have complementary information from multi-modal images. The quantitative evaluation mainly uses quality evaluation metrics to measure the performance of image fusion. We selected 6 popular metrics, including the MSE, PSNR, N_{abf} , gradient-based similarity measurement (Q_{abf}) (Xydeas and Petrovic 2000), SSIM (Wang et al. 2004) and SCD. We also evaluate the performance of the different methods on the typical downstream task, infrared-visible object detection, and semantic segmentation.

Evaluation on the FMB Dataset

Quantitative Comparisons. The quantitative results on the FMB dataset are summarized in Table 1. Our method outperforms 8 state-of-the-art approaches on three key metrics. Achieving the best scores in PSNR and N_{abf} on both the MSRS and FMB datasets demonstrates its consistent ability to preserve image clarity and reduce distortion across diverse scenarios. The top performance in Q_{abf} further indicates that our method effectively retains and integrates structural and textural information from the source images. A high N_{abf} score highlights strong gradient consistency and spatial coherence, which are crucial for vision-based tasks. These advantages make our method well-suited for downstream applications such as object detection.

Qualitative Comparisons. We mark the foreground region with the yellow rectangular box showing their zoomed-in effects for easier comparison in Fig. 3. Among all methods ex-

Methods	MSE	PSNR	Q_{abf}	N_{abf}	SSIM	SCD
FMB Dataset						
LDFusion	0.061	60.71	0.51	0.112	0.514	1.549
SwinFuse	0.042	62.334	0.577	<u>0.029</u>	0.905	1.9
NestFuse	<u>0.046</u>	61.96	0.483	0.042	0.787	1.594
CDDFuse	0.048	62.696	0.674	0.026	1.002	1.626
DIDFuse	0.047	61.565	0.528	0.042	0.765	1.824
SeAFusion	0.047	<u>62.539</u>	0.654	<u>0.029</u>	0.964	1.62
PSFusion	0.051	61.517	0.627	0.056	0.836	1.875
SDCFusion	0.048	62.456	0.693	0.031	0.906	<u>1.657</u>
CtrlFuse(Ours)	0.043	63.292	0.719	0.024	0.925	1.522
DroneVehicle Dataset						
LDFusion	0.076	59.573	0.376	0.054	0.568	1.38
SwinFuse	0.084	59.165	0.202	0.069	0.558	1.295
NestFuse	0.071	59.786	0.307	0.052	0.486	1.413
CDDFuse	0.065	60.199	0.469	0.021	<u>0.845</u>	1.359
DIDFuse	<u>0.067</u>	59.988	0.265	0.062	0.466	1.459
SeAFusion	0.094	58.649	<u>0.492</u>	<u>0.044</u>	0.879	1.472
PSFusion	0.067	<u>60.065</u>	0.454	0.095	0.717	1.534
SDCFusion	0.078	59.443	0.534	0.035	0.853	1.316
CtrlFuse(Ours)	0.063	60.317	0.496	0.035	0.779	1.552
MSRS Dataset						
LDFusion	0.056	61.05	0.438	0.116	0.541	1.515
SwinFuse	0.038	63.69	0.178	0.026	0.343	1.033
NestFuse	0.033	64.128	0.242	0.025	0.217	1.138
CDDFuse	0.038	<u>64.309</u>	0.689	<u>0.023</u>	1.001	1.623
DIDFuse	0.035	63.94	0.204	0.025	0.223	1.121
SeAFusion	<u>0.036</u>	64.491	0.675	0.021	0.982	1.707
PSFusion	0.037	64.001	0.676	0.042	0.917	1.812
SDCFusion	0.039	64.003	0.712	<u>0.023</u>	0.957	1.739
CtrlFuse(Ours)	0.035	64.75	0.685	0.018	0.969	1.726

Table 1: Quantitative comparison of CtrlFuse with 8 state-of-the-art methods. **Bold underline** indicates the best, **Bold** indicates the second best, and Underline indicates the third.

cept LDFusion and our proposed method, the fused images suffer from excessive brightness information in the truck’s windshield due to over-enhanced infrared information, resulting in blurry appearances. Only in the fused images produced by LDFusion and our method can the person inside the truck be clearly observed. Furthermore, our method better highlights the person, making them more distinguishable from the background.

Evaluation on the DroneVehicle Dataset

Quantitative Comparisons. Table 1 reports the performance of the different methods on the DroneVehicle dataset for 6 metrics, where our method achieves the best in 3 metrics. Among them, PSNR and MSE indicate that our method introduces minimal distortion and produces clearer and more detailed images with less noise interference. Moreover, the highest SCD indicates the method’s effectiveness in maintaining sharpness and clarity. These quantitative results indicate that the proposed CtrlFuse method can efficiently cap-

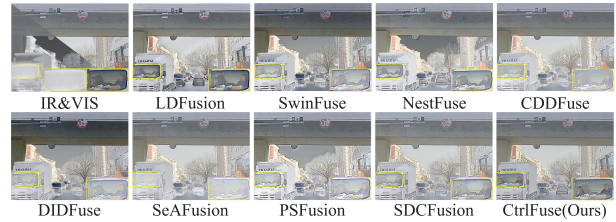


Figure 3: Qualitative comparisons of various methods on representative images selected from the FMB dataset.

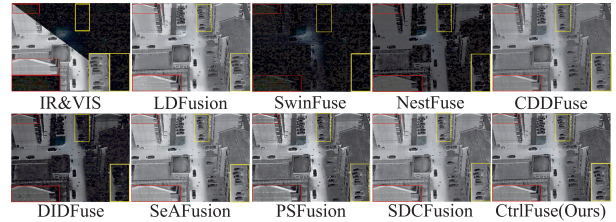


Figure 4: Qualitative comparisons of various methods on representative images selected from DroneVehicle dataset.

ture and integrate multi-modal information, leading to fusion outcomes that are both visually compelling and rich in detail.

Qualitative Comparisons. We mark the background regions with yellow and red boxes, respectively, in Fig. 4, with zoomed-in views provided for clearer comparison. As indicated by the yellow box, in the fused images of SwinFuse, NestFuse, and DIDFuse, excessive preference for the visible image makes the scene overly dark, rendering the cars in shadowed areas indistinguishable. As highlighted by the red box, LDFusion fails to adequately preserve texture details, causing the stripes on the exterior wall to be smoothed out, while SwinFuse and NestFuse still fail to distinguish the details due to insufficient infrared information. Our fused image achieves a superior balance between the infrared and visible input images.

High-level Vision Tasks Evaluation

Infrared and visible image fusion integrates information from different spectral bands to produce more informative and comprehensive representations, commonly used in high-level vision tasks like object detection, classification, and scene understanding. In this section, we conduct experiments on semantic segmentation and object detection.

Segmentation Performance. We conducted quantitative experiments on the MSRS dataset. Please refer to the supplementary material for detailed experimental settings. Segmentation performance, reported in Table 2, is evaluated using pixel-wise IoU. As shown, our method achieves the best performance on four categories and ranks second on four others, with the highest overall mIoU, indicating superior segmentation accuracy and generalization. We also provide visual results in Fig. 5. For the “car” class (purple), only our method achieved complete segmentation,

MSRS	Background	Car	Person	Bike	Curve	Car Stop	Guardrail	Color Tone	Bump	mIoU
Infrared	0.9669	0.7542	<u>0.5251</u>	0.7287	0.5926	0.7381	0.9763	0.7925	0.9299	0.7783
Visible	0.9658	0.7612	0.3904	0.7393	0.5664	0.7957	0.9797	0.7964	0.9414	0.7707
LDFusion	0.9667	0.6859	0.4463	0.7221	0.5078	0.7783	0.9837	0.7867	0.9404	0.7576
SwinFuse	0.9572	0.7013	0.4243	0.7090	0.5738	0.7757	0.9808	0.7561	0.9320	0.7567
NestFuse	0.9587	0.6844	0.4136	0.6938	0.5731	0.7758	0.9714	0.7434	0.9349	0.7499
CDDFuse	0.9696	0.7609	0.4856	0.7424	0.5843	0.7833	0.9829	0.7951	0.9375	0.7824
DIDFuse	0.9666	0.7471	0.4625	0.7268	0.5651	0.8009	0.9817	0.7807	0.9334	0.7739
SeAFusion	0.9695	0.7667	0.4886	0.7507	0.5991	0.7771	0.9822	0.7949	0.9395	0.7854
PSFusion	<u>0.9708</u>	<u>0.7722</u>	0.5276	0.7482	<u>0.6122</u>	0.7962	<u>0.9812</u>	0.8064	0.9443	0.7955
SDCFusion	0.9708	0.7682	0.5227	0.7420	0.6112	0.8028	0.9809	0.8121	0.9441	0.7950
CtrlFuse(Ours)	0.9705	0.7810	0.5134	0.7443	0.6179	0.8025	0.9851	0.8082	0.9438	0.7963

Table 2: Segmentation performance (mIoU) of visible, infrared and fused images on the MSRS dataset. **Bold** indicates the best, Underline indicates the second best.

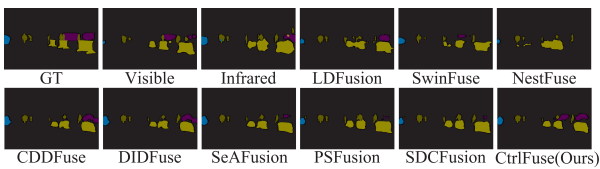


Figure 5: Segmentation results for infrared, visible, and fused images from the MSRS dataset. The segmentation models are retrained.

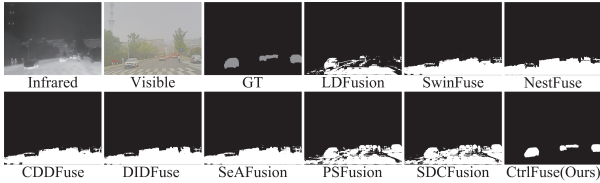


Figure 6: Segmentation results of the original SAM model and CtrlFuse on the FMB dataset.

further demonstrating its effectiveness in preserving critical semantic information for downstream tasks. We also evaluated DeepLabV3+ (Chen et al. 2018), pre-trained on Cityscapes (Cordts et al. 2016), on the FMB dataset, including the original dual-modal images, results from 8 SOTA methods, and our fused images. More details are provided in the supplementary material.

Detection Performance. Object detection is a fundamental and high-level task in computer vision that aims to identify and localize multiple objects within an image or video. To adapt the model to the DroneVehicle dataset, we selected the first 2000 images from the test set. Of these, 200 were randomly chosen for evaluation, and the remaining 1800 were used to fine-tune YOLOv5 on infrared-visible image pairs, improving its detection performance on this dataset. The fine-tuned YOLOv5 model was then used to evaluate fusion methods for object detection performance. The evaluation results are presented in Table 3, which shows the average performance over thresholds from 0.5 to 0.95

Method	car	truck	bus	freight car	All
LDFusion	0.632	0.409	0.475	0.324	0.460
SwinFuse	0.382	0.032	0.426	0.19	0.258
NestFuse	0.555	0.271	0.365	0.317	0.377
CDDFuse	0.632	0.455	0.470	0.387	0.486
DIDFuse	0.528	0.279	0.388	0.264	0.364
SeAFusion	0.646	0.458	<u>0.514</u>	0.415	0.508
PSFusion	0.628	0.475	0.424	0.277	0.451
SDCFusion	<u>0.647</u>	0.526	0.468	0.397	<u>0.510</u>
CtrlFuse(Ours)	0.651	<u>0.520</u>	0.521	0.409	0.525

Table 3: Object detection performance (AP@[0.5:0.95]) on the DroneVehicle dataset. **Bold** indicates the best, Underline indicates the second best.

(AP@[0.5:0.95]). As can be observed, the proposed method achieves the best performance in the “car” and “bus” categories, ranks second in the remaining categories, and maintains the highest overall metric (All), demonstrating its superior object detection accuracy across multiple evaluation criteria. In addition, we provide visual comparison results in the supplementary materials. We also provide a series of comparative experiments on downstream tasks without prompt masks in the supplementary materials.

Ablation Study

We conducted ablation studies on the MSRS dataset and reported the results in Table 4.

w/o Prompt. To investigate the impact of prompts on fusion quality, we remove the prompt mask from our framework, retaining only the two image encoders and a single decoder. The results in Table 4 show that, while the pixel-level fidelity remains similar, the perceptual quality and structural integrity are notably improved. This indicates that the prompt mask enhances the suitability of fused images for high-level vision tasks, with improvements in structural similarity, noise reduction, and spectral consistency likely benefiting downstream tasks such as object detection and semantic segmentation.

Ablation	MSE	PSNR	Q_{abf}	N_{abf}	SSIM	SCD
w/o Prompt	0.035	64.958	0.637	0.014	0.933	1.635
w/o Seg	0.036	64.615	<u>0.671</u>	0.021	<u>0.939</u>	1.636
w/o Vis	0.033	65.064	0.656	0.02	0.915	<u>1.681</u>
w/o Ir	0.034	<u>65.027</u>	0.67	0.019	0.938	1.622
Exchange SQ	0.034	64.917	0.661	0.021	0.924	1.659
CtrlFuse(Ours)	0.035	64.75	0.685	<u>0.018</u>	0.969	1.726

Table 4: Ablation study on the MSRS dataset. **Bold** indicates the best, Underline indicates the second best.

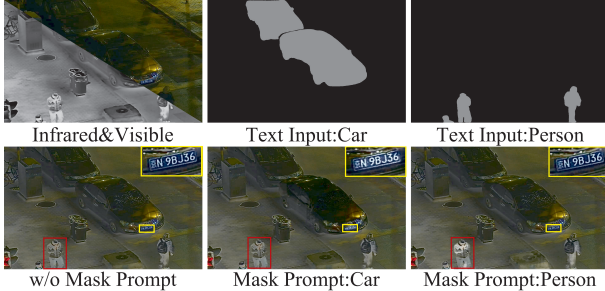


Figure 7: Fusion results of CtrlFuse with different prompt masks generated by Grounded-SAM on the LLVIP dataset.

w/o Seg. To verify that segmentation does not harm fusion performance, we remove the SAM mask decoder and the corresponding segmentation loss \mathcal{L}_{seg} . The resulting performance drop across all metrics demonstrates that segmentation improves fusion quality by preserving details, reducing noise, and maintaining structural and spectral integrity. Thus, segmentation plays a beneficial and essential role in achieving high-quality image fusion.

w/o Vis. To verify the contribution of both modalities, we remove the reference prompt encoder and prompt-semantic fusion module from the visible branch, eliminating the semantic prompt F_{vis}^p in fusion. While pixel-level fidelity slightly improves, the removal degrades perceptual quality and structural integrity, indicating that the visible prompt branch plays a key role in enhancing fusion performance.

w/o Ir. We perform the same ablation on the infrared branch by removing its corresponding components. A similar degradation in perceptual quality and structural integrity was observed, confirming that both modalities are crucial for high-quality image fusion.

Exchange SQ. To determine whether using F_{ir} or F_{vis} as the support feature is more effective, we swap the roles of support and query features in the reference prompt encoder. In the modified version, F_{ref} serves as the support feature, while F_{ir} or F_{vis} becomes the query. The overall drop in performance indicates that the original design is more effective for feature alignment and fusion.

Analysis and Discussion

The Impact of Mask Prompt Fine-tuning on SAM Performance. To investigate how the fusion branch enhances segmentation via prompt fine-tuning, we compared CtrlFuse

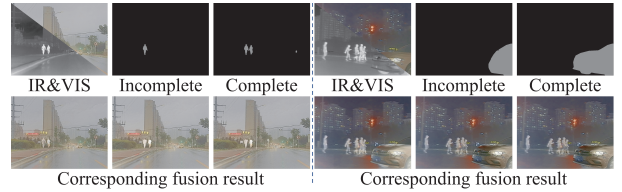


Figure 8: Comparison of fusion results under complete versus incomplete or coarse prompt masks.

with the original SAM and other fusion methods. As shown in Fig. 6, our method, which directly combines the segmentation masks from its two branches, achieves superior performance, demonstrating that the fine-tuned CtrlFuse enables more effective personalized segmentation guided by mask prompts.

Controllability of CtrlFuse. CtrlFuse uses prompt masks to guide the model to focus on and enhance specific targets. To validate this, we experimented on the LLVIP dataset (Jia et al. 2021), which lacks segmentation annotations. We employed Grounded-SAM (Ren et al. 2024) to generate masks from different text inputs and used them to guide the fusion process. The resulting images in Fig. 7 demonstrate the model’s capability to emphasize designated classes under varying conditions.

Sensitivity Analysis on Prompt Mask. Our analysis shows the model’s robustness to prompt mask quality. Even when masks are incomplete or of low quality (e.g., masking only one object or just a part of it), the fusion results still effectively highlight the target objects, including unmarked areas, as shown in Fig. 8. Visual comparisons confirm that mask quality has no significant impact on the output.

Conclusion

In this paper, we present CtrlFuse, a mask-prompt controllable multimodal image fusion framework that establishes dynamic interactions between scene understanding requirements and low-level fusion processes. By integrating mask-guided semantic adaptation with explicit feature fusion mechanisms, the proposed method addresses the critical limitation of conventional task-driven fusion approaches in rigid semantic constraints. Through synergistic design of the reference prompt encoder for adaptive semantic tuning, the prompt semantic fusion module for cross-modal feature aggregation, and the joint optimization of segmentation-aware fusion objectives, our framework achieves both semantically enhanced fusion results and improved downstream perception accuracy. Experimental validations across diverse scenarios demonstrate that the explicit injection of semantic guidance enables not only controllable fusion behavior but also mutual reinforcement between multimodal fusion and semantic segmentation tasks. The proposed paradigm provides an interactive and controllable multimodal fusion perception solution for intelligent unmanned systems, which is particularly suitable for all-weather search and rescue applications that require a focus on specific targets.

Acknowledgments

This work was supported by the National Natural Science Foundation of China under Grants 62222608, 62506073, and 62436002, the Tianjin Natural Science Funds for Distinguished Young Scholar under Grant 23JCJQJC00270, the Postdoctoral Fellowship Program of CPSF under Grant Number GZB20250395, the Jiangsu Funding Program for Excellent Postdoctoral Talent under Grant Number 2025ZB294, the the Zhejiang Provincial Natural Science Foundation of China under Grant LD24F020004.

References

Avrahami, O.; Lischinski, D.; and Fried, O. 2022. Blended diffusion for text-driven editing of natural images. In *Proceedings of the IEEE/CVF conference on computer vision and pattern recognition*, 18208–18218.

Cao, B.; Sun, Y.; Zhu, P.; and Hu, Q. 2023. Multi-Modal Gated Mixture of Local-to-Global Experts for Dynamic Image Fusion. In *Proceedings of the IEEE/CVF International Conference on Computer Vision*, 23555–23564.

Cao, P.; Zhou, F.; Song, Q.; and Yang, L. 2024. Controllable generation with text-to-image diffusion models: A survey. *arXiv preprint arXiv:2403.04279*.

Chen, L.-C.; Zhu, Y.; Papandreou, G.; Schroff, F.; and Adam, H. 2018. Encoder-decoder with atrous separable convolution for semantic image segmentation. In *Proceedings of the European conference on computer vision (ECCV)*, 801–818.

Cordts, M.; Omran, M.; Ramos, S.; Rehfeld, T.; Enzweiler, M.; Benenson, R.; Franke, U.; Roth, S.; and Schiele, B. 2016. The cityscapes dataset for semantic urban scene understanding. In *Proceedings of the IEEE conference on computer vision and pattern recognition*, 3213–3223.

Hoe, J. T.; Jiang, X.; Chan, C. S.; Tan, Y.-P.; and Hu, W. 2024. Interactdiffusion: Interaction control in text-to-image diffusion models. In *Proceedings of the IEEE/CVF Conference on Computer Vision and Pattern Recognition*, 6180–6189.

Huang, L.; Chen, D.; Liu, Y.; Shen, Y.; Zhao, D.; and Zhou, J. 2023. Composer: Creative and controllable image synthesis with composable conditions. *arXiv preprint arXiv:2302.09778*.

Hussain, M. 2024. Yolov1 to v8: Unveiling each variant—a comprehensive review of yolo. *IEEE access*, 12: 42816–42833.

Jia, X.; Zhu, C.; Li, M.; Tang, W.; and Zhou, W. 2021. LLVIP: A Visible-infrared Paired Dataset for Low-light Vision. In *Proceedings of the IEEE/CVF International Conference on Computer Vision (ICCV) Workshops*, 3496–3504.

Jiang, P.; Ergu, D.; Liu, F.; Cai, Y.; and Ma, B. 2022. A Review of Yolo algorithm developments. *Procedia computer science*, 199: 1066–1073.

Kirillov, A.; Mintun, E.; Ravi, N.; Mao, H.; Rolland, C.; Gustafson, L.; Xiao, T.; Whitehead, S.; Berg, A. C.; Lo, W.-Y.; et al. 2023. Segment anything. In *Proceedings of the IEEE/CVF international conference on computer vision*, 4015–4026.

Li, H.; Wu, X.-J.; and Durrani, T. 2020. NestFuse: An infrared and visible image fusion architecture based on nest connection and spatial/channel attention models. *IEEE Transactions on Instrumentation and Measurement*, 69(12): 9645–9656.

Liu, J.; Fan, X.; Huang, Z.; Wu, G.; Liu, R.; Zhong, W.; and Luo, Z. 2022. Target-aware Dual Adversarial Learning and a Multi-scenario Multi-Modality Benchmark to Fuse Infrared and Visible for Object Detection. In *Proceedings of the IEEE/CVF Conference on Computer Vision and Pattern Recognition (CVPR)*, 5802–5811.

Liu, J.; Li, X.; Wang, Z.; Jiang, Z.; Zhong, W.; Fan, W.; and Xu, B. 2024a. PromptFusion: Harmonized semantic prompt learning for infrared and visible image fusion. *IEEE/CAA Journal of Automatica Sinica*.

Liu, J.; Liu, Z.; Wu, G.; Ma, L.; Liu, R.; Zhong, W.; Luo, Z.; and Fan, X. 2023. Multi-interactive feature learning and a full-time multi-modality benchmark for image fusion and segmentation. In *Proceedings of the IEEE/CVF international conference on computer vision*, 8115–8124.

Liu, J.; Wu, G.; Liu, Z.; Wang, D.; Jiang, Z.; Ma, L.; Zhong, W.; Fan, X.; and Liu, R. 2025. Infrared and Visible Image Fusion: From Data Compatibility to Task Adaption. *IEEE Transactions on Pattern Analysis and Machine Intelligence*, 47(4): 2349–2369.

Liu, X.; Huo, H.; Li, J.; Pang, S.; and Zheng, B. 2024b. A semantic-driven coupled network for infrared and visible image fusion. *Information Fusion*, 108: 102352.

Ma, J.; Chen, C.; Li, C.; and Huang, J. 2016. Infrared and visible image fusion via gradient transfer and total variation minimization. *Information Fusion*, 31: 100–109.

Ma, J.; Ma, Y.; and Li, C. 2019. Infrared and visible image fusion methods and applications: A survey. *Information fusion*, 45: 153–178.

Ma, J.; Xu, H.; Jiang, J.; Mei, X.; and Zhang, X.-P. 2020. DDcGAN: A dual-discriminator conditional generative adversarial network for multi-resolution image fusion. *IEEE Transactions on Image Processing*, 29: 4980–4995.

Ma, J.; Yu, W.; Liang, P.; Li, C.; and Jiang, J. 2019. FusionGAN: A generative adversarial network for infrared and visible image fusion. *Information Fusion*, 48: 11–26.

Radford, A.; Kim, J. W.; Hallacy, C.; Ramesh, A.; Goh, G.; Agarwal, S.; Sastry, G.; Askell, A.; Mishkin, P.; Clark, J.; et al. 2021. Learning transferable visual models from natural language supervision. In *International conference on machine learning*, 8748–8763. PMLR.

Ren, T.; Liu, S.; Zeng, A.; Lin, J.; Li, K.; Cao, H.; Chen, J.; Huang, X.; Chen, Y.; Yan, F.; Zeng, Z.; Zhang, H.; Li, F.; Yang, J.; Li, H.; Jiang, Q.; and Zhang, L. 2024. Grounded SAM: Assembling Open-World Models for Diverse Visual Tasks. *arXiv:2401.14159*.

Shi, Y.; Xue, C.; Liew, J. H.; Pan, J.; Yan, H.; Zhang, W.; Tan, V. Y.; and Bai, S. 2024. Dragdiffusion: Harnessing diffusion models for interactive point-based image editing. In *Proceedings of the IEEE/CVF Conference on Computer Vision and Pattern Recognition*, 8839–8849.

Sun, Y.; Cao, B.; Zhu, P.; and Hu, Q. 2022a. Delfusion: A detection-driven infrared and visible image fusion network. In *Proceedings of the 30th ACM International Conference on Multimedia*, 4003–4011.

Sun, Y.; Cao, B.; Zhu, P.; and Hu, Q. 2022b. Drone-Based RGB-Infrared Cross-Modality Vehicle Detection Via Uncertainty-Aware Learning. *IEEE Transactions on Circuits and Systems for Video Technology*, 32: 6700–6713.

Sun, Y.; Cao, B.; Zhu, P.; and Hu, Q. 2024a. Dynamic brightness adaptation for robust multi-modal image fusion. In *Proceedings of the Thirty-Third International Joint Conference on Artificial Intelligence*, 1317–1325.

Sun, Y.; Chen, J.; Zhang, S.; Zhang, X.; Chen, Q.; Zhang, G.; Ding, E.; Wang, J.; and Li, Z. 2024b. VRP-SAM: SAM with visual reference prompt. In *Proceedings of the IEEE/CVF Conference on Computer Vision and Pattern Recognition*, 23565–23574.

Sun, Y.; Li, X.; Zhu, P.; Hu, Q.; Ren, D.; Xu, H.; and Zhu, X. 2025. Task-Gated Multi-Expert Collaboration Network for Degraded Multi-Modal Image Fusion. In *Proceedings of the 42nd International Conference on Machine Learning*, volume 267, 57571–57586. PMLR.

Tang, L.; Deng, Y.; Yi, X.; Yan, Q.; Yuan, Y.; and Ma, J. 2024. DRMF: Degradation-Robust Multi-Modal Image Fusion via Composable Diffusion Prior. In *Proceedings of the ACM International Conference on Multimedia*, 8546–8555.

Tang, L.; Li, C.; and Ma, J. 2025. Mask-DiFuser: A Masked Diffusion Model for Unified Unsupervised Image Fusion. *IEEE Transactions on Pattern Analysis and Machine Intelligence*, 1–18.

Tang, L.; Wang, Y.; Cai, Z.; Jiang, J.; and Ma, J. 2025a. ControlFusion: A Controllable Image Fusion Framework with Language-Vision Degradation Prompts. *Advances in Neural Information Processing Systems*.

Tang, L.; Yan, Q.; Xiang, X.; Fang, L.; and Ma, J. 2025b. C2RF: Bridging Multi-modal Image Registration and Fusion via Commonality Mining and Contrastive Learning. *International Journal of Computer Vision*, 133: 5262–5280.

Tang, L.; Yuan, J.; and Ma, J. 2022. Image fusion in the loop of high-level vision tasks: A semantic-aware real-time infrared and visible image fusion network. *Information Fusion*, 82: 28–42.

Tang, L.; Yuan, J.; Zhang, H.; Jiang, X.; and Ma, J. 2022. PIAFusion: A progressive infrared and visible image fusion network based on illumination aware. *Information Fusion*, 83-84: 79–92.

Tang, L.; Zhang, H.; Xu, H.; and Ma, J. 2023. Rethinking the necessity of image fusion in high-level vision tasks: A practical infrared and visible image fusion network based on progressive semantic injection and scene fidelity. *Information Fusion*, 99: 101870.

Wang, Y.; Miao, L.; Zhou, Z.; Zhang, L.; and Qiao, Y. 2024. Infrared and visible image fusion with language-driven loss in CLIP embedding space. *arXiv preprint arXiv:2402.16267*.

Wang, Z.; Bovik, A. C.; Sheikh, H. R.; and Simoncelli, E. P. 2004. Image quality assessment: from error visibility to structural similarity. *IEEE transactions on image processing*, 13(4): 600–612.

Wang, Z.; Chen, Y.; Shao, W.; Li, H.; and Zhang, L. 2022. SwinFuse: A Residual Swin Transformer Fusion Network for Infrared and Visible Images. *IEEE Transactions on Instrumentation and Measurement*, 1–1.

Wu, G.; Liu, H.; Fu, H.; Peng, Y.; Liu, J.; Fan, X.; and Liu, R. 2025. Every SAM Drop Counts: Embracing Semantic Priors for Multi-Modality Image Fusion and Beyond. *arXiv preprint arXiv:2503.01210*.

Xydeas, C. S.; and Petrovic, V. S. 2000. Objective image fusion performance measure. *Electronics Letters*, 36: 308–309.

Yi, X.; Xu, H.; Zhang, H.; Tang, L.; and Ma, J. 2024. Text-if: Leveraging semantic text guidance for degradation-aware and interactive image fusion. In *Proceedings of the IEEE/CVF Conference on Computer Vision and Pattern Recognition*, 27026–27035.

Zhang, H.; Xu, H.; Tian, X.; Jiang, J.; and Ma, J. 2021. Image fusion meets deep learning: A survey and perspective. *Information Fusion*, 76: 323–336.

Zhang, L.; and Agrawala, M. 2024. Transparent image layer diffusion using latent transparency. *arXiv preprint arXiv:2402.17113*.

Zhao, Z.; Bai, H.; Zhang, J.; Zhang, Y.; Xu, S.; Lin, Z.; Timofte, R.; and Van Gool, L. 2023. Cddfuse: Correlation-driven dual-branch feature decomposition for multi-modality image fusion. In *Proceedings of the IEEE/CVF conference on computer vision and pattern recognition*, 5906–5916.

Zhao, Z.; Xu, S.; Zhang, C.; Liu, J.; Zhang, J.; and Li, P. 2020. DIDFuse: Deep Image Decomposition for Infrared and Visible Image Fusion. In *Proceedings of the Twenty-Ninth International Conference on International Joint Conferences on Artificial Intelligence*, 970–976. ijcai.org.

Appendices.

Fusion Evaluation Metric

MSE. The Mean Squared Error (MSE) is a commonly used image quality evaluation metric. It calculates the average of the squared differences between the corresponding pixel values of the original and processed images. Assuming the original image I and the fused image J both have a size of $M \times N$, the Mean Squared Error (MSE) can be defined as:

$$MSE = \frac{1}{MN} \sum_{i=1}^M \sum_{j=1}^N [I(i, j) - J(i, j)]^2. \quad (8)$$

The lower the MSE, the better the fused image is in terms of similarity to the source images. A lower MSE indicates less distortion and more accurate preservation of details and information from the source images.

PSNR. The Peak Signal-to-Noise Ratio (PSNR) is a widely used image quality evaluation metric. It is based on the Mean Squared Error (MSE) and reflects the ratio between the maximum possible signal intensity and the noise intensity in an image.

$$PSNR = 10 \log_{10} \left(\frac{MAX^2}{MSE} \right), \quad (9)$$

where MAX^2 is the square of the maximum pixel value in the fused image. The higher the PSNR, the more effectively the fused image retains the quality and integrity of the source images. A high PSNR suggests superior visual fidelity, indicating successful preservation of original details and minimal loss or distortion during the fusion process.

Q_{abf} . Q_{abf} refers to a specific image quality evaluation metric, commonly used to measure the similarity and fusion effectiveness between fused images and source images. It comprehensively considers multiple aspects of image information, such as brightness, contrast, and structure. By calculating similarity measures between the fused image and the source images in different feature spaces, and then combining them through weighted summation, Q_{abf} produces an overall quality assessment score. It can be calculated as:

$$Q_{abf} = \frac{1}{N} \sum_{i=1}^N w_i \frac{(2\mu_{a,i}\mu_{b,i} + C_1)}{(\mu_{a,i}^2 + \mu_{b,i}^2 + C_1)} \cdot \frac{(2\sigma_{a,b,i} + C_2)}{(\sigma_{a,i}^2 + \sigma_{b,i}^2 + C_2)}, \quad (10)$$

where N is the number of image blocks, w_i is the weight of the i -th image block, $\mu_{a,i}$ and $\mu_{b,i}$ are the means of the i -th image block in source images a and b , respectively, $\sigma_{a,i}^2$ and $\sigma_{b,i}^2$ are the variances of the i -th image block in source images a and b , respectively, $\sigma_{a,b,i}$ is the covariance of the i -th image block in source images a and b , and C_1 and C_2 are constants. A higher Q_{abf} indicates more effective information transfer and better visual performance of the fused image, reflecting a well-balanced fusion outcome with minimal degradation.

N_{abf} . N_{abf} correlates with factors including the image's noise level and the extent of detail retention. It assesses image quality by analyzing and quantifying characteristics

such as noise properties and high-frequency detail information within the image.

$$N_{abf} = \frac{1}{N} \sum_{i=1}^N w_i \frac{\sigma_{n,i}}{\sigma_{a,b,i} + C}, \quad (11)$$

where N is the number of image blocks, w_i is the weight of the i -th image block, $\sigma_{n,i}$ is the standard deviation of the noise in the i -th image block, $\sigma_{a,b,i}$ is the covariance of the i -th image block in source images a and b , and C is a small constant used to prevent division by zero. A lower N_{abf} reflects a higher-quality fused image with less noise and fewer artifacts, making it clearer and more faithful to the source images.

SCD. The Sum of Correlation Differences is a metric used to measure the differences between fused images and source images as a way to characterize the quality of the fusion algorithm.

$$SCD = \sum_{i=1}^N w_i |\rho_{a,i} + \rho_{b,i} - 2\rho_{f,i}|, \quad (12)$$

where N is the number of image blocks. w_i is the weight of the i -th image block. $\rho_{a,i}$ and $\rho_{b,i}$ are the correlation coefficients of the i -th block in source images a and b , respectively. $\rho_{f,i}$ is the correlation coefficient of the i -th block in the fused image. A higher SCD indicates that the fused image contains richer information from the source images.

SSIM. SSIM evaluates image quality based on three components: luminance (mean intensity), contrast (variance), and structural similarity (correlation). It is defined as:

$$SSIM(x, y) = \frac{(2\mu_x\mu_y + C_1)(2\sigma_{xy} + C_2)}{(\mu_x^2 + \mu_y^2 + C_1)(\sigma_x^2 + \sigma_y^2 + C_2)}, \quad (13)$$

where μ_x and μ_y are the averages of the pixel values in the two images (representing luminance). σ_x^2 and σ_y^2 are the variances of the pixel values in the two images (representing contrast). σ_{xy} is the covariance between the two images (representing structural similarity or correlation). C_1 and C_2 are small constants added to stabilize the division with a weak denominator. An increase in SSIM suggests that the fused image better captures the structural characteristics of the source images, leading to a result that appears more visually consistent and natural to human observers.

Model Details

In the CtrlFuse method, both the infrared and visible image encoders utilize Gradient Residual Dense Blocks (GRDB) proposed in (Tang, Yuan, and Ma 2022). In addition to the Gradient Residual Dense Blocks (GRDB), the encoders also consist of convolutional layers and activation layers. The detailed structure of the image encoders is shown in Fig. 9. The decoder module is implemented as a sequence of ConvLeakyRelu2d layers. The channel dimensions are successively halved (aside from the final step) through the network, following the pattern: $256 \rightarrow 128 \rightarrow 64 \rightarrow 32 \rightarrow 16 \rightarrow 1$, to ultimately generate a single-channel output.

In addition, our model utilizes a frozen SAM model, specifically `sam_vit_h_4b8939`. The image decoder is composed of convolutional layers and activation layers.

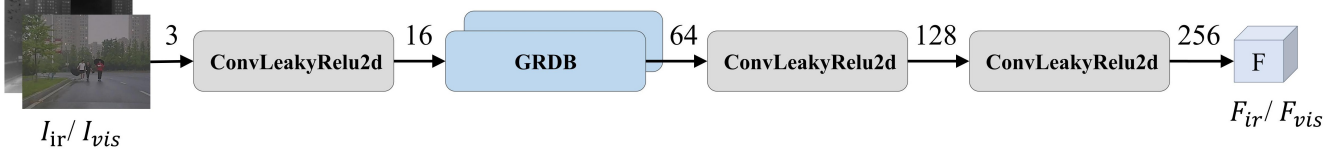


Figure 9: The architecture of CtrlFuse Image Encoder. Encoder consists of GRDB, convolutional layers, and activation layers.



Figure 10: Qualitative comparisons of various methods on representative images selected from the MSRS dataset.

Methods	MSE	PSNR	Q_{abf}	N_{abf}	SSIM	SCD
LDFusion	0.056	61.05	0.438	0.116	0.541	1.515
SwinFuse	0.038	63.69	0.178	0.026	0.343	1.033
NestFuse	0.033	64.128	0.242	0.025	0.217	1.138
CDDFuse	0.038	<u>64.309</u>	0.689	<u>0.023</u>	1.001	1.623
DIDFuse	0.035	63.94	0.204	0.025	0.223	1.121
SeAFusion	<u>0.036</u>	64.491	0.675	0.021	0.982	1.707
PSFusion	0.037	64.001	0.676	0.042	0.917	<u>1.812</u>
SCDFusion	0.039	64.003	<u>0.712</u>	<u>0.023</u>	0.957	1.739
CtrlFuse(Ours)	0.035	64.75	<u>0.685</u>	0.018	0.969	1.726

Table 5: Quantitative comparison of our CtrlFuse with 8 state-of-the-art methods on the MSRS dataset. **Bold underline** indicates the best performance, **bold** the second best, and underline the third best.

Hyperparameter Experiment about the Learnable Query

In the RPE module, we introduce a set of learnable query vectors Q to steer the attention mechanism toward the target regions specified by the prompts. To determine the optimal number of query vectors N , we conduct a series of hyperparameter experiments. Given the primary role of Q in refining the segmentation outputs from SAM to produce more accurate binary masks, we adopt the mIoU trend with respect to N as the selection criterion. As shown in Fig. 12 depicting mIoU versus N , the model achieves optimal performance when $N = 40$, which is consequently chosen as the final configuration.

Loss Function

In CtrlFuse, we use $\mathcal{L}_{\text{fusion}}$ to guide the optimization of the image fusion network, and the segmentation branch is fine-tuned through the segmentation loss \mathcal{L}_{seg} . The entire framework is trained end-to-end by jointly optimizing the two loss functions. Therefore, the overall loss is defined as:

$$\mathcal{L}_{\text{total}} = \mathcal{L}_{\text{fusion}} + \mathcal{L}_{\text{seg}}. \quad (14)$$

Specifically, $\mathcal{L}_{\text{fusion}}$ can be calculated as:

$$\mathcal{L}_{\text{fusion}} = \mathcal{L}_{\text{pixel}} + \mathcal{L}_{\text{grad}} + \mathcal{L}_{\text{int}} + \mathcal{L}_{\text{percep}}, \quad (15)$$

where $\mathcal{L}_{\text{pixel}}$ (Sun et al. 2022a) is composed of two components: one for the object regions and another for the background region. It can be described as:

$$\begin{aligned} \mathcal{L}_{\text{pixel}} = & \frac{1}{HW} \|I_{\text{seg}} \cdot (I_F - \max(I_{\text{vis}}, I_{\text{ir}}))\|_1 \\ & + \frac{1}{HW} \|(1 - I_{\text{seg}}) \cdot (I_F - \text{mean}(I_{\text{vis}}, I_{\text{ir}}))\|_1, \end{aligned} \quad (16)$$

where H and W are the height and width of an image, respectively, $\|\cdot\|_1$ stands for the ℓ_1 -norm, and I_{seg} represents the segmentation results obtained from the two branches. The gradient loss plays a crucial role in improving the structural quality and visual fidelity of the fused image, focusing on preserving spatial gradients. We define the gradient loss of infrared and visible images as:

$$\mathcal{L}_{\text{grad}} = \frac{1}{HW} \|\nabla I_F - \max(\nabla I_{\text{vis}}, \nabla I_{\text{ir}})\|_1. \quad (17)$$

The intensity loss is used to preserve the pixel-wise brightness information and ensure visual fidelity between

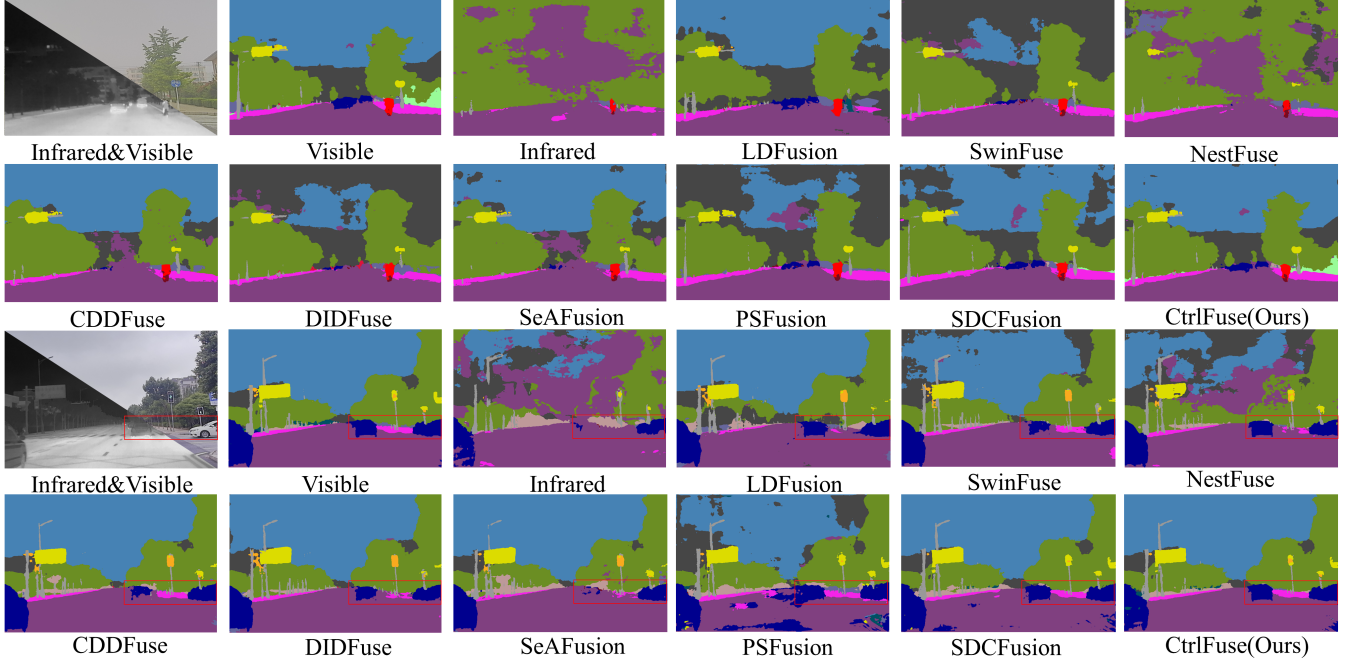


Figure 11: Segmentation results for infrared, visible, and fused images from the FMB dataset. The segmentation model is Deeplabv3+, pre-trained on the Cityscapes dataset.

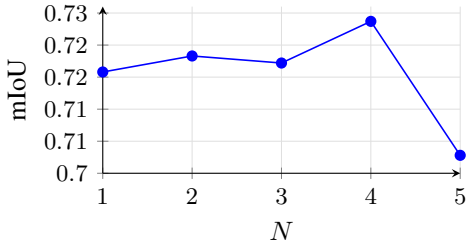


Figure 12: Hyperparameter Optimization of Query Vector Count in RPE Module

the fused image and the source images. Therefore, we define the intensity loss of infrared and visible images as:

$$\mathcal{L}_{int} = \frac{1}{HW} \|I_F - \max(I_{ir}, I_{vis})\|_1. \quad (18)$$

The perceptual loss enhances the visual realism and structural fidelity of fused images by aligning their deep features with those of the source images. \mathcal{L}_{percep} can be defined as:

$$\begin{aligned} \mathcal{L}_{percep} = & \sum_{l \in L} \frac{1}{N_l} \|\Phi_l(I_F) - \Phi_l(I_{ir})\|_2^2 \\ & + \sum_{l \in L} \frac{1}{N_l} \|\Phi_l(I_F) - \Phi_l(I_{vis})\|_2^2, \end{aligned} \quad (19)$$

where $\Phi_l(\cdot)$ represents the feature map obtained from the l -th layer of the pre-trained VGG model, N_l is the normalization factor corresponding to the number of elements in

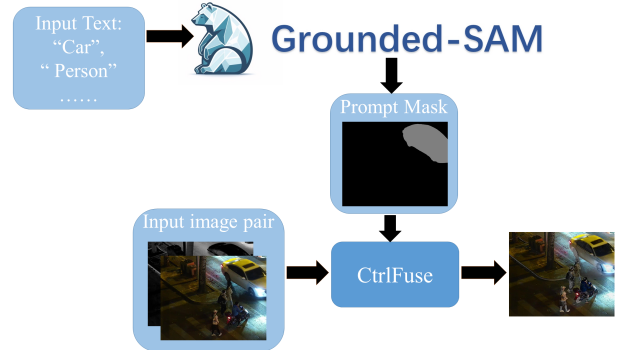


Figure 13: Inference pipeline with Prompt Mask.

the feature map, and $\|\cdot\|_2^2$ denotes the squared L2 norm, which is equivalent to the mean squared error.

Ablation studies on the perceptual loss confirm its effectiveness in enhancing both the visual realism and structural fidelity of the fusion results. The corresponding quantitative results are presented in Table 6.

Method	MSE	PSNR	Qabf	Nabf	SSIM	SCD
w/o \mathcal{L}_{percep}	0.046	62.922	0.715	0.033	0.912	1.434
CtrlFuse (Ours)	0.043	63.292	0.719	0.024	0.925	1.522

Table 6: Ablation study on perceptual loss.

We employ the Binary Cross-Entropy (BCE) loss and Dice loss to jointly supervise the segmentation learning pro-

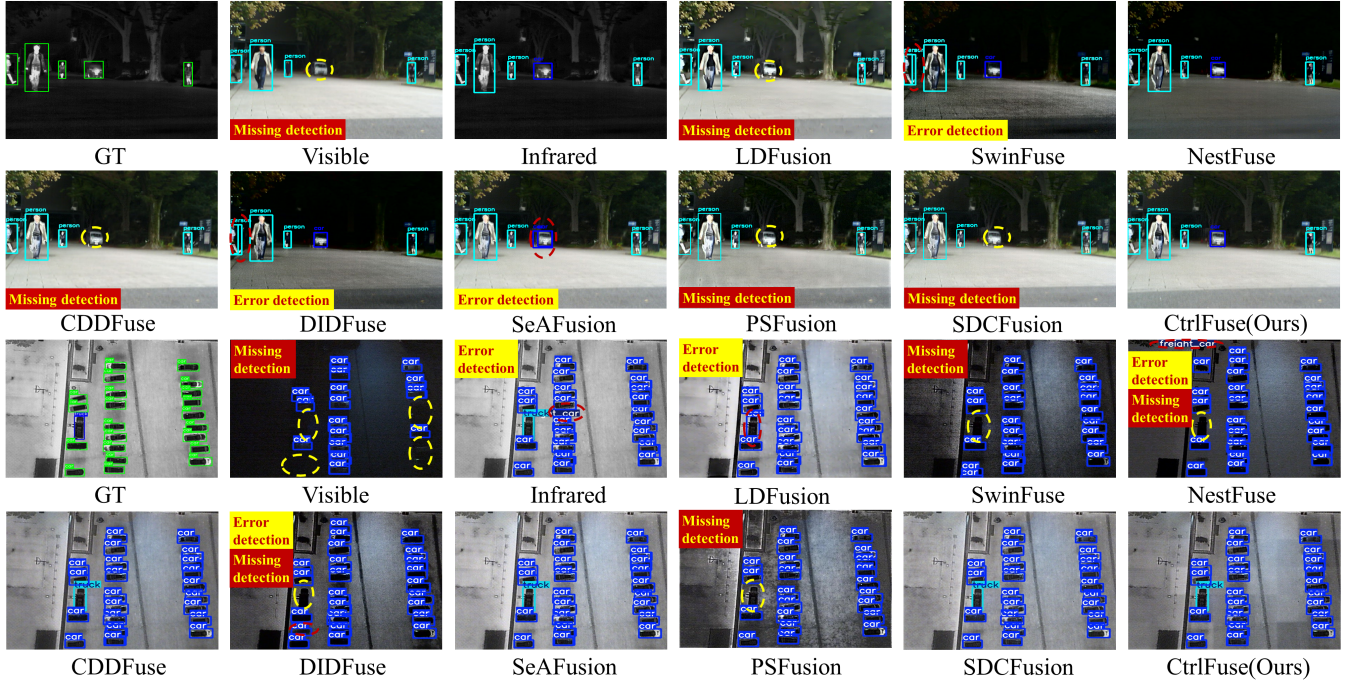


Figure 14: Object detection results for infrared, visible, and fused images from the MSRS and DroneVehicle dataset.

cess. Therefore we can define \mathcal{L}_{seg} as:

$$\mathcal{L}_{\text{seg}} = \mathcal{L}_{\text{BCE}} + \mathcal{L}_{\text{dice}}, \quad (20)$$

$$\mathcal{L}_{\text{BCE}} = -\frac{1}{N} \sum_{i=1}^N [y_i \log (\hat{y}_i) + (1 - y_i) \log (1 - \hat{y}_i)], \quad (21)$$

$$\mathcal{L}_{\text{dice}} = 1 - \frac{2 \sum_{i=1}^N (\hat{y}_i \cdot y_i)}{\sum_{i=1}^N \hat{y}_i^2 + \sum_{i=1}^N y_i^2}, \quad (22)$$

where y_i is the ground-truth label for the i -th pixel, \hat{y}_i is the predicted probability for the i -th pixel, and N is the total number of pixels.

Evaluation on the MSRS dataset

Quantitative Comparisons. Table 5 presents the results of the quantitative evaluation on the MSRS dataset, where our method achieves the best performance in two metrics and ranks second and third in the remaining metrics, respectively. In particular, CtrlFuse attains the highest values for PSNR and N_{abf} , indicating its superior performance in preserving image quality and structural details. The highest PSNR value further corroborates this, as it reflects excellent pixel-level similarity. The lowest N_{abf} value highlights the method’s effectiveness in minimizing blurring and maintaining high-resolution image quality.

Qualitative Comparisons. We mark the foreground region with the yellow rectangular box. We also show their zoomed-in effects for easier comparison in Fig. 10. In LDFusion, the over-reliance on thermal signals in foreground regions disrupts background texture preservation, causing artifacts such as blurred or distorted vehicles. Our method

addresses this by adaptively suppressing redundant thermal interference while maintaining visible modality details, ensuring balanced multi-modal fusion. In SwinFuse, NestFuse, and DIDFuse, excessive contrast enhancement in thermal regions leads to over-darkening of visible details, severely weakening the saliency of target objects. This imbalance causes critical features to become indistinct due to overly suppressed luminance.

Ablation Study

In this ablation study, we removed the RPE and PSFM modules, retaining only the SAM as the segmentation component. Under this configuration, SAM directly performs multi-class semantic segmentation without requiring input prompt masks. The semantic masks generated by the two branches are normalized and fused with their respective extracted features via Hadamard product, then added to the reference feature F_{ref} to obtain the final fused feature. The rest of the model architecture remains unchanged. The final quantitative results are presented in Table 7.

Method	MSE	PSNR	Qabf	Nabf	SSIM	SCD
w/o RPE&PSFM	0.049	62.682	0.691	0.039	0.895	1.463
CtrlFuse (Ours)	0.043	63.292	0.719	0.024	0.925	1.522

Table 7: Quantitative results of the ablation study on RPE and PSFM modules.

Method	Background	Car	Person	Bike	Curve	Car Stop	Guardrail	Color	Tone	Bump	mIoU
w/o Mask Prompt	0.9704	0.7698	0.5125	0.7531	0.6156	0.8026	0.9850	0.8066	0.9447	0.7956	
CtrlFuse(Ours)	0.9705	0.7810	0.5134	0.7443	0.6179	0.8025	0.9851	0.8082	0.9438	0.7963	

Table 8: Quantitative comparison of segmentation performance with and without mask prompts on the MSRS dataset. **Bold** indicates the best.

High-level Vision Tasks Evaluation

Segmentation Performance. We conducted quantitative experiments on the MSRS dataset. We retrained the DeepLabV3+ semantic segmentation models for both the dual-modal image pairs and nine fusion methods, including our approach, using identical parameters throughout the training process. We employ DeepLabV3+ with a ResNet backbone, setting the initial learning rate to 0.01 and utilizing a single GPU for training. The model is configured to train over 200 epochs with a batch size of 11.

Moreover, we evaluate the performance of DeepLabV3+, pre-trained on the Cityscapes dataset, on both the original dual-modal images, the fused results generated by eight state-of-the-art fusion methods, and our proposed fused images on the FMB dataset. This experimental setup allows for a comprehensive comparison of how different fusion strategies impact downstream semantic segmentation performance. Given that the Cityscapes dataset is composed of visible light imagery, the visible images can be used as an approximate ground truth for evaluation purposes. In Fig. 11, focusing on the sky portion of FMB image 01431, it is evident that the semantic segmentation result obtained from our fusion method is closer to the visible image. Similarly, on the vehicle portion of FMB image 01382, our fused image achieves a more complete segmentation result.

Detection Performance. We conducted object detection experiments on the MSRS detection dataset using the pre-trained YOLOv8 model (Jiang et al. 2022; Hussain 2024). Before testing, we used GroundedSAM to segment the detection set to obtain prompt masks. We provide several visual examples in Fig. 14 to demonstrate the effectiveness of our fusion algorithm in enhancing object detection performance. In the MSRS scene 583, the detector fails to detect a car from the Visible, LDFusion, CDDFuse, PSFusion, and SDCFuse images. While SwinFuse and DIDFuse produce error detections of an additional person, SeAFusion incorrectly identifies an extra vehicle. In DroneVehicle image 151, false detections are observed in the infrared, LD-Fusion, NestFuse, and DIDFuse images. Additionally, missing detections occur in the visible images, as well as with SwinFuse, NestFuse, DIDFuse, and PSFusion. In these two sets of examples, only our method successfully avoids both error detections and missing detections. This demonstrates that our method provides sufficient semantic information for high-level vision tasks.

Comparison of CtrlFuse with and without Mask Prompts. Our method is an interactive and controllable fusion algorithm. During the inference phase, we employ GroundedSAM to interactively generate mask prompts to guide the model learning as shown in Fig. 13, while also sup-

Metrics	mAP on DroneVehicle Dataset				
	car	truck	bus	freight car	All
AP@0.5					
w/o Mask Prompt	0.929	0.591	0.674	0.413	0.652
CtrlFuse(Ours)	0.952	0.639	0.708	0.533	0.708
AP@0.7					
w/o Mask Prompt	0.826	0.560	0.642	0.405	0.608
CtrlFuse(Ours)	0.877	0.597	0.708	0.519	0.675
AP@[0.5:0.95]					
w/o Mask Prompt	0.618	0.420	0.454	0.315	0.451
CtrlFuse(Ours)	0.651	0.521	0.521	0.409	0.525

Table 9: Object detection performance comparison on the DroneVehicle dataset with and without mask prompts. Metrics include mAP@0.5, mAP@0.7, and mAP@[0.5:0.95] for car, truck, bus, freight car, and overall (All) classes. **Bold** indicates the best.

porting prompt-free input. To verify the contribution of our method with prompt masks in downstream tasks, we compare its performance with and without prompt masks on semantic segmentation and object detection.

In Table 8, we present the semantic segmentation test metrics of the method without Prompt Mask and our method on the MSRS dataset. Following the same semantic segmentation experimental setup as before, we conduct testing using retrained DeepLabV3+ semantic segmentation models. Our method achieves improvements over the no-prompt approach in six categories and demonstrates superiority in mIoU. To provide a more intuitive comparison, we also offer visual comparisons as shown in Fig 15. We provide a visual comparison of segmentation results in four scenarios. In the first row (MSRS 00862N), our method successfully segments the “curve” region, while the no-prompt approach fails. In the second row (MSRS 00874N), the distant “person” is not detected by the no-prompt method, whereas our method manages to segment a partial region of the person. In the third row (MSRS 00931N), the no-prompt method loses the semantic information of the “car” due to overexposure, while our method obtains an incomplete but recognizable segmentation mask. In the fourth row, the target is a person riding a bicycle; the no-prompt method fails to segment the bicycle, while our method successfully captures it. These visual comparisons further demonstrate that our prompt-guided fusion method is more effective in preserving semantic information.

In Table 9, we present the object detection test metrics

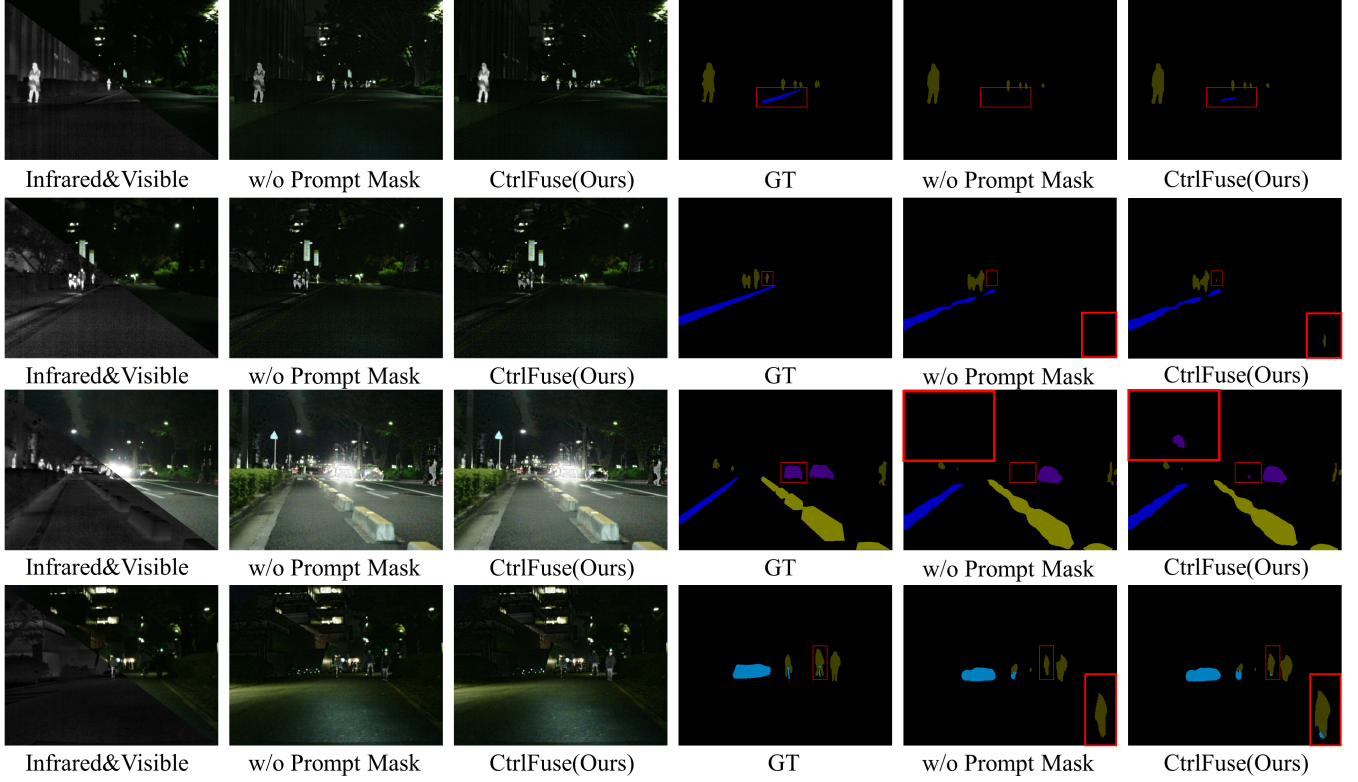


Figure 15: Qualitative comparisons of segmentation performance with and without mask prompts on the MSRS dataset.

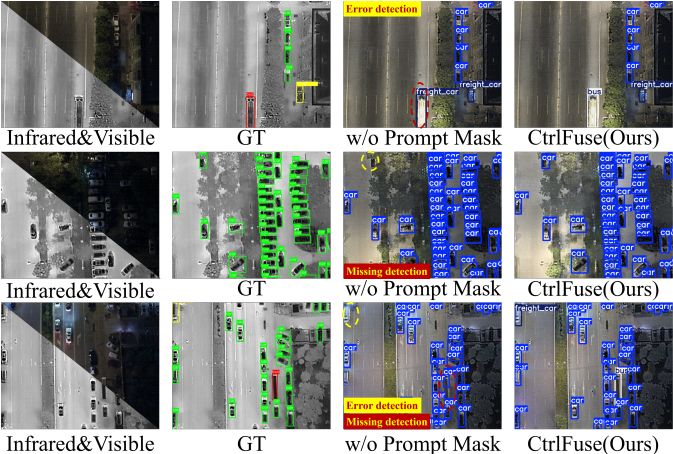


Figure 16: Qualitative comparisons of object detection performance with and without mask prompts on the DroneVehicle dataset.

of the method without Prompt Mask and our method on the DroneVehicle dataset. Our method performs better than the method without Mask Prompt across all metrics. In addition, we have also provided qualitative comparisons as shown in Fig. 16. In the first row, scene 423 of DroneVehicle, the method without Prompt Mask misclassifies a “bus” as a “freight car”. In the second row, scene 1064 of DroneVehicle

fails, the prompt-free method fails to detect a car. In the third row, scene 1373, the prompt-free method misses a freight car and misclassifies a bus as a car. Through quantitative and qualitative analysis, the fusion method guided by the mask prompt significantly outperforms the non-prompted approach in object detection. This further demonstrates that prompt guidance enables the algorithm to focus more on our designated regions of interest and enriches the detailed information.

Comparison with SAM-based Fusion Method SAGE

Wu et al. (Wu et al. 2025) proposed a fusion method that utilizes semantic priors from the SAM for IVIF. In this subsection, we conduct both qualitative and quantitative analyses in comparison with SAGE.

Comparison on the FMB Dataset. Qualitative comparisons were performed on the FMB dataset, as illustrated in Fig. 17. In the first column of images, we use red and yellow rectangles to mark the two foreground objects, respectively, and magnify these areas for easier comparison. We focus on the details of car hubs. Infrared images provide rich brightness and texture, whereas visible images mainly capture texture. In SAGE’s fused results, texture is obscured by dominant brightness information, causing blurry edges and reduced detail. Our method better balances the integration of this information, preserving texture clarity and edge sharpness. In the second to fourth columns, we use yellow rectan-

Method	Background	Car	Person	Bike	Curve	Car Stop	Guardrail	Color Tone	Bump	mIoU
SAGE	0.970	0.777	0.498	0.743	0.613	0.797	0.985	0.812	0.945	0.793
CtrlFuse (Ours)	0.971	0.781	0.513	0.744	0.618	0.802	0.985	0.808	0.944	0.796

Table 10: Quantitative comparison on semantic segmentation task with SAGE method. **Bold** indicates the best.

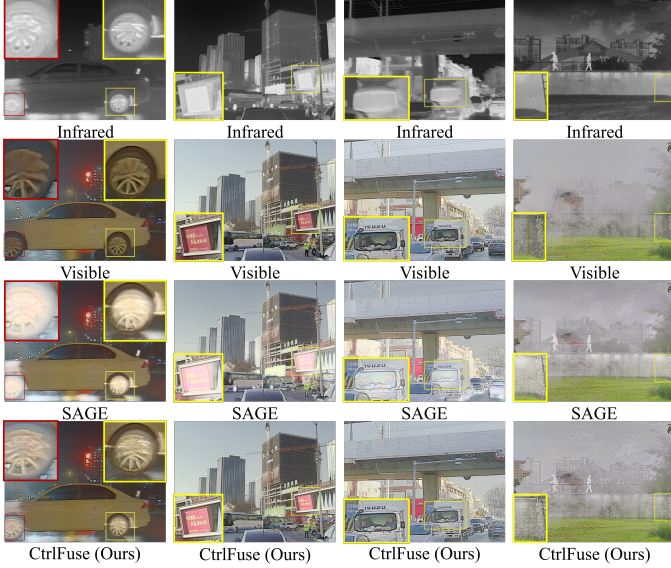


Figure 17: Qualitative comparisons with SAGE on representative images selected from the FMB dataset.

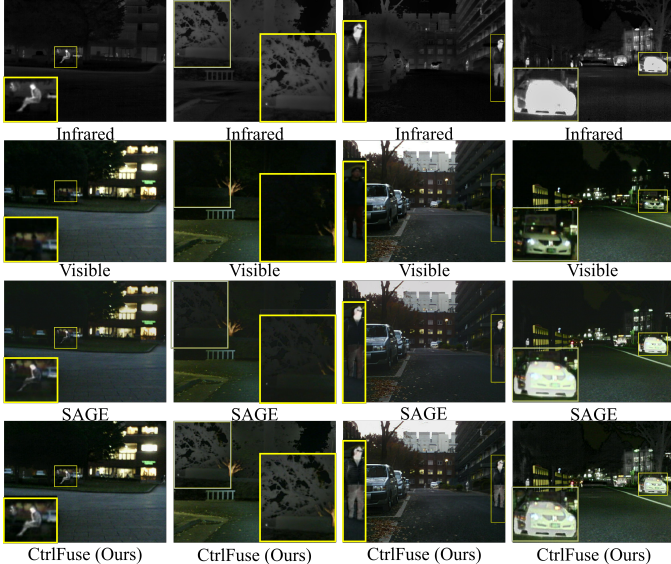


Figure 18: Qualitative comparisons with SAGE on representative images selected from the MSRS dataset.

gular boxes to highlight the targets and zoom in on these areas for detailed comparison. These columns respectively focus on a signboard (second), a person within a truck (third),

Method	MSE	PSNR	Q_{abf}	N_{abf}	SSIM	SCD
SAGE	0.09	58.844	0.336	0.035	0.677	1.413
CtrlFuse(Ours)	0.063	60.317	0.496	0.035	0.779	1.552

Table 11: Comparison of SAGE and CtrlFuse Methods on the DroneVehicle dataset. **Bold** indicates the optimal metric values.

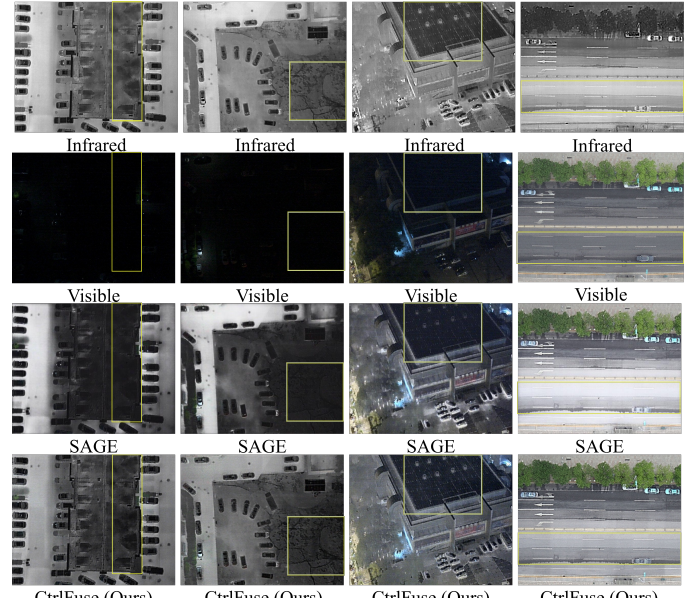


Figure 19: Qualitative comparisons with SAGE on representative images selected from the DroneVehicle dataset.

and wall stains (fourth). The cases presented in the second to fourth columns represent daytime scenarios, in which infrared features play a more supplementary role. Nevertheless, the SAGE fusion method introduces an overemphasis on infrared characteristics, resulting in significant texture degradation. Our approach, by comparison, achieves a more balanced integration that effectively retains the textual information.

Comparison on the MSRS Dataset. We conducted qualitative analyses on the MSRS dataset, as shown in Fig. 18. The first and third columns emphasize the human figures within the scenes. In such cases, the thermal information corresponding to ‘person’ becomes a key focus of analysis. As illustrated in the figure, the SAGE fusion method introduces extraneous information from the visible images into the ‘person’ regions in both examples. This interference

Methods	Object Detection Performance					
	car	truck	bus	freight car	All	
AP@0.5						
SAGE	0.922	0.659	0.591	0.430	0.651	
CtrlFuse (Ours)	0.952	0.639	0.708	0.533	0.708	
AP@[0.5:0.95]						
SAGE	0.627	0.491	0.419	0.337	0.468	
CtrlFuse (Ours)	0.651	0.521	0.521	0.409	0.525	

Table 12: Object detection performance comparison with SAGE method. **Bold** indicates superior performance.

leads to a degradation of thermal detail, making the thermal information less prominent. In contrast, our method effectively preserves the thermal characteristics. The second and fourth columns highlight the textural details of branches and cars, respectively. In the second column, SAGE places excessive emphasis on the visible image, causing the branch textures to become indistinct. In the fourth column, however, an overemphasis on the infrared image leads to the attenuation of visible information, which results in a loss of clarity in the car’s front section. Relative to SAGE, our approach excels in balancing the image features from both infrared and visible modalities. By appropriately combining the thermal information from infrared images with the detailed textures from visible images, our method retains clarity and detail in both aspects.

Method	MSE	PSNR	Qabf	Nabf	SSIM	SCD
Reference Fusion	0.046	62.96	0.717	0.029	0.917	1.46
CtrlFuse (Ours)	0.043	63.292	0.719	0.024	0.925	1.522

Table 13: Quantitative comparison between the reference fusion and our final output.

Comparison on the DroneVehicle Dataset. The quantitative results on the DroneVehicle dataset are shown in Table 11. Our method outperforms SAGE on five evaluation metrics, while achieving comparable performance on the sixth. The high PSNR and SSIM values of fused images indicate superior visual quality and detail preservation, while lower MSE ensures accurate information retention. Enhanced Q_{abf} scores improve the clarity of blurred frames, aiding reliable tracking and detection. Improved SCD performance allows precise identification of spectral changes, beneficial for distinguishing subtle environmental differences.

To clearly distinguish the object regions, we annotate them with a yellow rectangular box in Fig. 19. In the first three columns of the comparison images, SAGE’s inability to balance primary and auxiliary features leads to amplified interference. This results in the fused images being biased towards visible image information, causing important features to be lost. Conversely, as shown in the final set of comparison images, SAGE tends to over-enhance the brightness information derived from the infrared input, which results



Figure 20: The fusion results obtained with the “**car**” **mask prompt** at varying control parameter levels are shown from left to right: no mask prompt, 1× prompt, 5× prompt, and 10× prompt.



Figure 21: The fusion results obtained with the “**person**” **mask prompt** at varying control parameter levels are shown from left to right: no mask prompt, 1× prompt, 5× prompt, and 10× prompt.

in the suppression of road landmarks and surface textures due to excessive brightness. In contrast, our method avoids over-amplifying information from a single modality, which can lead to information loss. Instead, it effectively balances information from both modalities, ensuring that no critical details are obscured.

Comparisons on Semantic Segmentation. To further validate the semantic extraction capability of our method, we conducted comparative experiments with SAGE, another SAM-based approach, on the semantic segmentation task. Quantitative results are presented in Table 10. The superior performance on the majority of classes and in mIoU demonstrates an enhanced utilization of SAM’s semantic comprehension capabilities by our method.

Comparisons on Object Detection. To further validate the effectiveness of our method on downstream tasks, we compare its object detection performance with SAGE. As quantitatively demonstrated in Table 12, our approach achieves superior results across nearly all evaluation metrics. This outcome further confirms the enhanced capability of our method in leveraging semantic information for improved object detection.

Controllable Fusion Details

During testing, we can alter the fused image by controlling the fusion parameters, allowing the highlighted regions to

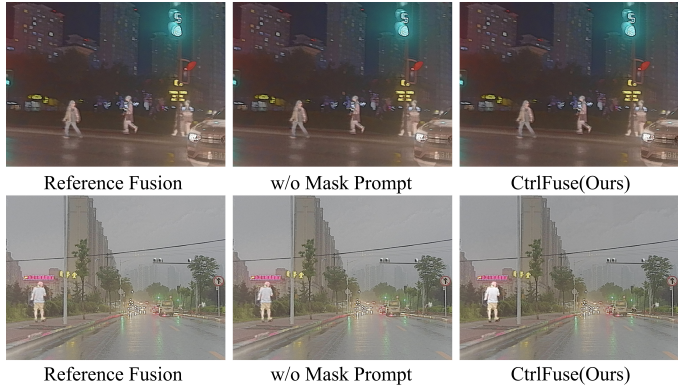


Figure 22: Qualitative comparison of the reference fusion image, prompt-free result, and our prompt-based fusion result.

appear at different levels of prominence. In the Fig. 20 and Fig. 21, we demonstrate examples of the “car” and “person” classes using “no prompt”, “1x prompt”, “5x prompt”, and “10x prompt” to illustrate the effects of prompt features. As can be seen in the two examples, the prompted regions in the fused images become increasingly prominent from left to right. In the case of the “car” example as Fig. 20, increasing the intensity of the prompt feature primarily enhances the visible characteristics, resulting in clearer texture details. In the first row, as the intensity of the prompt is increased, the vehicle in the frame contains richer texture detail (sharper license plate numbers), and in the second row, the detail of the vehicle in the far distance is sharper. In the “person” example illustrated in Fig. 21, the fusion results progressively favor infrared information as we move from left to right. As the intensity of the prompt increases, the pedestrians in the first and second rows of images possess more significant contrast in nighttime conditions. In the two experiments mentioned above, we further validated that the fusion algorithm we proposed features interactive controllability.

Comparison of Fusion Result with the Reference Fusion Image

The intermediate fusion result I_{ref} is generated during the process and serves as a reference fusion image for subsequent modules. Its primary role is to provide a query mechanism that guides the entire fusion process toward the desired optimization direction. We conducted both quantitative and qualitative comparisons between I_{ref} and I_F , with the results detailed in Table 13 and Fig. 22, respectively. As can be observed from the qualitative comparison figures, the reference fusion map exhibits similarity to the fusion results without mask prompt.